Pulling Back the Curtain on Shocks and Star Formation in NGC 1266 with Gemini-NIFS

(article starts on next page)

Pulling Back the Curtain on Shocks and Star Formation in NGC 1266 with Gemini-NIFS

Justin Atsushi Otter[1], Katherine Alatalo[1,2], Kate Rowlands[1,3], Richard M. McDermid[4,5], Timothy A. Davis[6], Christoph Federrath[5,7], K. Decker French[8], Timothy Heckman[1,9], Patrick Ogle[2], Darshan Kakkad[2], Yuanze Luo[1], Kristina Nyland[10], Akshat Tripathi[8], Pallavi Patil[1], Andreea Petric[2], Adam Smercina[11], Maya Skarbinski[1], Lauranne Lanz[12], Kristin Larson[2], Philip N. Appleton[13], Susanne Aalto[14], Gustav Olander[14], Elizaveta Sazonova[15], and J. D. T. Smith[16]

[1] William H. Miller III Department of Physics and Astronomy, Johns Hopkins University, Baltimore, MD 21218, USA; jotter2@jhu.edu
[2] Space Telescope Science Institute, 3700 San Martin Drive, Baltimore, MD 21218, USA
[3] AURA for ESA, Space Telescope Science Institute, 3700 San Martin Drive, Baltimore, MD 21218, USA
[4] Astrophysics and Space Technologies Research Centre, School of Mathematical and Physical Sciences, Macquarie University, Sydney, NSW 2109, Australia
[5] ARC Centre of Excellence for All Sky Astrophysics in 3 Dimensions (ASTRO 3D), Australia
[6] Cardiff Hub for Astrophysics Research & Technology, School of Physics & Astronomy, Cardiff University, Queens Buildings, Cardiff, CF24 3AA, UK
[7] Research School of Astronomy and Astrophysics, Australian National University, Canberra, ACT 2611, Australia
[8] Department of Astronomy, University of Illinois, 1002 W. Green Street, Urbana, IL 61801, USA
[9] School of Earth and Space Exploration, Arizona State University, Temple, AZ 85287, USA
[10] U.S. Naval Research Laboratory, 4555 Overlook Ave SW, Washington, DC 20375, USA
[11] Astronomy Department, University of Washington, Seattle, WA 98195, USA
[12] Department of Physics, The College of New Jersey, Ewing, NJ 08628, USA
[13] Caltech/IPAC, MC 314-6, 1200 E. California Blvd., Pasadena, CA 91125, USA
[14] Department of Space, Earth and Environment, Chalmers University of Technology, 412 96 Gothenburg, Sweden
[15] Department of Physics and Astronomy, University of Waterloo, 200 University Avenue West, Waterloo, ON N2L 3G1, Canada
[16] Ritter Astrophysical Research Center, Department of Physics and Astronomy, University of Toledo, Toledo, OH 43606, USA

Abstract

We present Gemini near-infrared integral field spectrograph K-band observations of the central 400 pc of NGC 1266, a nearby ($D \approx 30$ Mpc) post-starburst galaxy with a powerful multiphase outflow and a shocked interstellar medium. We detect seven H_2 rovibrational emission lines excited thermally to $T \sim 2000$ K, and weak Brγ emission, consistent with a fast continuous shock (or C-shock). With these bright H_2 lines, we observe the spatial structure of the shock with an unambiguous tracer for the first time. The Brγ emission is concentrated in the central $\lesssim 100$ pc, indicating that any remaining star formation in NGC 1266 is in the nucleus, while the surrounding cold molecular gas has little ongoing star formation. Though it is unclear what fraction of this Brγ emission is from star formation or the active galactic nuclei (AGN), assuming it is entirely due to star formation we measure an instantaneous star formation rate of $0.7 \, M_\odot \, \mathrm{yr}^{-1}$, though the star formation rate may be significantly higher in the presence of additional extinction. NGC 1266 provides a unique laboratory to study the complex interactions between AGN, outflows, shocks, and star formation, all of which are necessary to unravel the evolution of the post-starburst phase.

Unified Astronomy Thesaurus concepts: AGN host galaxies (2017); Shocks (2086); Near infrared astronomy (1093); Galaxy quenching (2040)

1. Introduction

The relationship between a galaxy and its supermassive black hole holds many of the keys to unlocking how galaxies evolve over cosmic time. Accreting supermassive black holes release enormous amounts of energy in the form of radiation-pressure-driven winds from the accretion disk or via collimated radio jets (e.g., A. C. Fabian 2012; T. M. Heckman & P. N. Best 2014, 2023). The connection between these actively accreting supermassive black holes and star formation in their host galaxies is often referred to as active galactic nuclei (AGN) feedback. Though feedback can be positive (instigating star formation), negative feedback (suppressing star formation) is necessary in theoretical work to regulate star formation and to reproduce the galaxy stellar mass function and the low overall star formation efficiency in the Universe (e.g., G. Kauffmann et al. 1999;

T. Di Matteo et al. 2005; P. F. Hopkins et al. 2006; M. Vogelsberger et al. 2014; J. Schaye et al. 2015). Direct observational evidence of AGN feedback has mostly centered on massive elliptical galaxies, and while indirect evidence exists in lower-mass galaxies, direct evidence is scant and results are mixed (e.g., D. C. Martin et al. 2007; K. Schawinski et al. 2010; V. Wild et al. 2010; A. C. Fabian 2012; E. Cheung et al. 2016; N. Roy et al. 2018; R. J. Smethurst et al. 2018; K. D. French et al. 2018). Further, much work remains to build a precise physical understanding of the connections and interplay between the black hole accretion, the interstellar medium (ISM), and star formation in galaxies.

Outflows are one of the clearest mechanisms by which an AGN interacts with the host galaxy on kiloparsec scales, though their impact on the host galaxy's ISM and star formation is unclear. Substantial observational and theoretical evidence demonstrates that large-scale outflows and jets can slowly quench the host galaxy by heating the surrounding circumgalactic medium, thus preventing further cold-gas accretion and ending star formation once the gas reservoirs

are depleted (e.g., L. Bîrzan et al. 2004; M. Gaspari et al. 2011; R. Morganti et al. 2013; R. Weinberger et al. 2017). However, the impacts of smaller kiloparsec-scale outflows on the host galaxy's ISM remain uncertain. While some outflows have sufficient velocity and mass to effectively remove the gas reservoirs from the host galaxy (N. P. H. Nesvadba et al. 2007; C. M. Harrison et al. 2014; D. S. N. Rupke et al. 2017), other outflows will not escape the host galaxy (K. Alatalo et al. 2015; J. A. Fernández-Ontiveros et al. 2020; Y. Luo et al. 2022). Still, these nonejective outflows can have important impacts on the galaxy's star formation properties as they can heat and drive turbulence into the ISM (N. P. H. Nesvadba et al. 2010, 2011; P. Guillard et al. 2012; A. Mandal et al. 2021), though it is not apparent whether this heating can impact star formation across the entire galaxy (J. M. Gabor & F. Bournaud 2014; H.-J. Bae et al. 2017)

Theoretical and observational work has shown that the turbulence and shock properties in molecular gas are key in determining the star formation efficiency of that gas. Supersonic turbulence and resulting shocks create compressions in the gas, widening the distribution of gas densities. While the high-density gas created by these compressions is ripe for star formation, turbulent stirring motions counteract star formation by hindering gravitational collapse (C. Federrath & R. S. Klessen 2012). The relationship between turbulence and star formation is primarily driven by the virial parameter of the gas (2 times the ratio of turbulent to gravitational energy), the sonic Mach number (the ratio of velocity dispersion to sound speed), and the driving mode of the turbulence (the ratio of the compressive and solenoidal, or stirring, modes).

Both galactic and extragalactic observational studies demonstrate that the physical processes which impact these turbulence parameters can effectively suppress star formation. Molecular clouds in the central molecular zone of the Milky Way have low star formation rates for the molecular gas mass, which may be caused by solenoidal-mode turbulence driven by shear forces (C. Federrath et al. 2016; A. T. Barnes et al. 2017). In an extragalactic context, D. M. Salim et al. (2020) show that the observed star formation suppression in NGC 7674 is consistent with an escalated virial parameter and solenoidal-mode turbulence driven by shear forces from the stellar bar and dense group environment. High turbulent pressures have been observed in other post-starburst galaxies, though further observations are necessary to directly link this turbulence to the ongoing star formation suppression (A. Smercina et al. 2022).

The relationships between AGN, radio jets, outflows, and the host galaxy's ISM and star formation form a complex, interconnected web. While progress has been made in studying individual connections in this web, an integrated understanding of the entire system is lacking. NGC 1266 provides an ideal laboratory for beginning to unpack these relationships in detail. NGC 1266 is a nearby ($D = 29.9$ Mpc, $1'' = 0.14$ kpc) post-starburst galaxy with a powerful multiphase outflow and a sizable molecular gas reservoir. Though NGC 1266 visually appears to be a typical S0 galaxy, CO observations reveal a large, centrally concentrated molecular gas reservoir ($1.7 \times 10^9\ M_\odot$) and a molecular outflow, achieving a molecular outflow mass rate of $110\ M_\odot\ \mathrm{yr}^{-1}$ (K. Alatalo et al. 2011, 2015). Despite high molecular gas surface densities and the presence of dense gas in the central region, there is little ongoing star formation, as the total star formation rate is suppressed by a factor of 10–100 times

from what is expected of the molecular gas mass using the Kennicutt–Schmidt relation (K. Alatalo et al. 2015). The outflow is multiphase, including ionized, atomic, molecular, and dense molecular gas components (T. A. Davis et al. 2012). The orientation of the outflow is similar to extended radio emission, which may be tracing relativistic radio jets from the AGN (K. Nyland et al. 2013). It is likely that an obscured, low-luminosity AGN drives this outflow, potentially through radio jets, as the outflow mass rate far exceeds even the most generous star formation rate measurements, and the radio jets have sufficient power to drive the outflow (K. Nyland et al. 2013; K. Alatalo et al. 2015).

The impact of the outflow on the ISM of NGC 1266 remains a critical open question necessary to understand the role of AGN feedback in this galaxy. Both the ionized gas emission lines and highly excited molecular transitions (CO, H_2O) demonstrate that the ISM is dominated by shocks (T. A. Davis et al. 2012; E. W. Pellegrini et al. 2013). While the powerful outflow is an intuitive driver of these shocks, the lack of spatially resolved observations of the shock features prevents definitive statements on the nature of the interactions between the outflow and ISM. Further, previous studies suggest that outflow-driven turbulence is suppressing star formation in the molecular gas, though high-spatial-resolution observations of the outflow and shocks are necessary to verify this scenario (K. Alatalo et al. 2015).

In NGC 1266, we aim to uncover the relationship between the outflow, ISM, and star formation, and thus the physics underlying AGN feedback. Spatially resolved near-infrared (NIR) integral field spectroscopy observations provide a crucial path toward this goal, as these data provide important constraints on the shock, molecular gas, and star formation properties of the ISM. Bright NIR rovibrational H_2 emission lines trace warm ($T \gtrsim 1000$ K) molecular gas, which can be heated by star formation, around H II regions, and by non-star-forming processes, such as shocks. Thermal excitation sources for H_2 include shocks and UV or X-ray radiation, which collisionally excite the gas, whereas UV or X-ray fluorescence are the primary nonthermal excitation mechanisms (e.g., J. H. Kwan et al. 1977; S. Lepp & R. McCray 1983; A. Sternberg 1989; B. T. Draine & D. T. Woods 1990; R. A. Dors et al. 2012; V. U et al. 2019). Nonthermal excitation mechanisms may still yield thermalized $\nu = 1$ states (i.e., (1–0) rovibrational emission lines), though the $\nu = 2$ states (i.e., (2–1) emission) will be more populated than would be expected from the $\nu = 1$ column densities.

As differing star formation tracers yield a wide range of star formation rates in NGC 1266, NIR hydrogen recombination lines provide a unique star formation constraint. This variance of measured star formation rates likely arises from the differing timescales probed by different methods. While some methods, such as hydrogen recombination lines, measure star formation on <10 Myr timescales, other methods, such as the far-infrared luminosity, measure the integrated star formation rate over a much longer period of time, which may include the recent burst of star formation in a post-starburst galaxy (K. D. French 2021). NIR hydrogen recombination lines, such as Brγ, provide a reliable, instantaneous star formation tracer less impeded by dust than their optical counterparts. The combination of Brγ and H_2 rovibrational lines further allows us to determine whether the Brγ we observe is dominated by shocks.

Table 1
Details of Each Observing Session with NIFS

Date	Exposure Length	Exposures	Total Exposure Time	Number of Dithers	Uncorrected V-band Seeing	Calibration Standard Stars
2014 10 Nov	600 s	7	4200 s	4	0″33	HIP10512
2015 31 Jan	600 s	6	3600 s	4	0″49	HIP10512, HIP22923
2015 1 Feb	600 s	11	6600 s	6	0″69	HIP10512, HIP22923

In this work, we present adaptive-optics-enhanced K-band observations taken with the Gemini Near-Infrared Integral Field Spectrograph (NIFS) of the central 400 pc of NGC 1266, covering multiple H_2 rovibrational transitions as well as the hydrogen recombination line Brγ. In Section 2, we provide details of these observations and data reduction. In Section 3, we present our emission-line measurements and plot various line diagnostics. We discuss possible H_2 excitation mechanisms, shock properties and structure, and the nuclear properties in Section 4, and share our conclusions in Section 5. When computing distances and scales, we adopt a Hubble constant of $H_0 = 70\ \mathrm{km\ s^{-1}\ Mpc^{-1}}$, $\Omega_m = 0.3$, and $\Omega_\Lambda = 0.7$.

2. Observations and Methods

2.1. Gemini-NIFS Observations and Reduction

Near-infrared observations of NGC 1266 were obtained with NIFS with laser guide star adaptive optics enabled on the Gemini North Telescope (P. J. McGregor et al. 2003; J. C. Christou et al. 2010) under program ID GN-2013B-Q-30 (PI: McDermid). These observations were taken with the K-band grating (central wavelength $\lambda = 2.2\ \mu m$) in three observing sessions from 2014 November to 2015 February. The NIFS field of view is $3'' \times 3''$ with an angular sampling of $0''103 \times 0''043$. The final science cubes are rebinned to a square pixel size of $0''043$. The spectral resolution of NIFS in the K band is $R \sim 5290$. With adaptive optics, NIFS observations typically achieve spatial resolutions of $0''1$–$0''2$.

Our observing strategy was as follows. In each observing session, an A-type star was observed immediately before NGC 1266 at a comparable air mass to facilitate the correction of telluric absorption. Each science exposure was 600 s, with a total of 24 exposures split across the three nights, for a total exposure time of 4 hr. Science exposures in each observing session were dithered to minimize the impact of bad detector pixels. Immediately after science observations, Ar and Xe arc-lamp calibration exposures were taken for wavelength calibration. In the latter two observing sessions, a different A-type star was additionally observed immediately after science observations. Other standard calibration exposures were taken including flat fields, darks, and a Ronchi calibration mask exposure to account for spatial distortion. More details on each observing session are provided in Table 1.

The data were reduced with `Nifty4Gemini`, a python pipeline built upon Gemini IRAF (M. Lemoine-Busserolle et al. 2019). The primary reduction steps for the science observations include coadding the science frames, performing sky subtraction, identifying and interpolating over bad pixels, computing spatial and wavelength distortion maps, correcting for telluric lines, flux-calibrating the cube, and finally merging the resulting science data from each observing visit. The

wavelength solution is determined from the arc-lamp exposures. Telluric corrections are performed with the A-type star observations. The flux is calibrated by fitting a blackbody function to the observed A-type star spectrum at a known temperature, and then scaling the blackbody function to the previous measured Two Micron All Sky Survey (2MASS) magnitude of the star. The flux calibration of NIFS is accurate to approximately 10%, as stated in the online documentation.[17]

The automatically generated offset values for merging data cubes in the pipeline were not accurate, so we specified integer pixel offsets manually. We determined these offsets by comparing the isophotes of continuum emission in each cube. The merging was performed with the pipeline, which uses the `imcombine` IRAF task to combine the cubes. This task only accepts integer pixel offsets, so we could not merge the cubes with subpixel accuracy. We had to merge both the cubes for different dither positions in each observing session, as well as the resulting three cubes from each observing session into one final science-ready data cube. Due to the manual offset specification, the final merged cube lacked absolute astrometry information. We register the NIFS data to accompanying F160W (H-band) Hubble Space Telescope (HST) imaging from K. Alatalo et al. (2014) by matching isophotes of the continuum emission. We assume the peak of the H-band continuum from HST is coincident with the NIFS K-band continuum, which is likely given they are both in the NIR.

Lastly, we find sharp absorption features in specific channels due to poor sky subtraction on each observing night. None of these features fall on the peak of detected emission lines, so we mask these channels in our analysis and do not expect them to have a significant impact on our results.

2.2. Spectral Fitting

To accurately model the stellar continuum, we use the `pPXF` python package, an implementation of the penalized pixel-fitting method of M. Cappellari (2023), building upon previous versions of the algorithm (M. Cappellari & E. Emsellem 2004; M. Cappellari 2017). We use the X-shooter spectral library (XSL) Data Release 3 as stellar templates (K. Verro et al. 2022). This library consists of 830 high-resolution ($R \sim 10,000$) stellar spectra of 683 stars. These spectra span UV to NIR wavelengths, from 0.35 to 2.480 μm, fully encompassing the wavelength range of our NIFS observations. We exclude XSL spectra which have not been corrected for wavelength-dependent slit flux loss, and spectra which were not corrected for galactic extinction, resulting in 670 remaining spectra. Stars in XSL were chosen to span as much of the Hertzsprung–Holland diagram as possible with a wide range of chemical compositions. Cool and otherwise

---

[17] https://www.gemini.edu/observing/resources/near-ir-resources

IR-luminous stars are emphasized, making XSL an ideal choice for NIR stellar continuum fitting. When fitting the stellar continuum, we mask regions around H_2 emission lines and $Br\gamma$. To model the observed stellar continuum as closely as possible, we include an additive and multiplicative Legendre polynomial of degree 10 to account for template mismatch.

At the ends of the wavelength range, above $2.42\,\mu m$ and below $2.025\,\mu m$, the fitted continuum sharply increases due to the multiplicative Legendre polynomial. Because this upturn in the stellar continuum heavily impacts our measured flux of the $H_2(1-0)\,Q(1)$ line, we instead use the median of the spectrum from 2.405 to $2.419\,\mu m$ as a flat continuum value. This wavelength range is adjacent to the $H_2(1-0)\,Q(1)$ line and is free from major emission and absorption features. We note that the measured fluxes of the $H_2(1-0)\,Q(1)$ line are less reliable due to this less precise continuum fitting method. We similarly replace the continuum below $2.025\,\mu m$ with the median value in the line-free region of $2.025-2.043\,\mu m$.

To measure emission-line properties, we fit emission lines using the following procedure. We perform a one-component and two-component Gaussian fit on the continuum-subtracted spectrum. We use the trust region reflective fitting algorithm, a nonlinear least-squares fitting method, as implemented by `scipy`. To determine whether a second Gaussian component represents a statistical improvement over the single-component fit, we compute the Bayesian information criterion, assuming Gaussian errors as

$$BIC = n \ln\left(\frac{SSR}{n}\right) + k \ln(n), \tag{1}$$

where n is the number of observations, SSR is the sum of squared residuals between the model and observations, and k is the degrees of freedom in the model. To accept the two-component model, we require

$$BIC_1 - BIC_2 > 10, \tag{2}$$

where BIC_1 and BIC_2 correspond to the one- and two-component models, respectively. The BIC for each model is not informative; only the difference between the two values provides a heuristic for which model better suits the data. We use a threshold value of 10, indicating there is very strong evidence that a second Gaussian component is needed to adequately represent the data (e.g., S. Mukherjee et al. 1998). From visual inspection, this threshold value matches by-eye determinations of whether one or two components are needed.

We compute uncertainties for our fluxes by measuring the standard deviation of a line-free continuum-subtracted region of the spectrum from 2.26 to $2.35\,\mu m$. We use the same spectral region for all of our uncertainties because some of our lines are in spectral regions with closely spaced emission lines, making it difficult to reliably measure the standard deviation of these regions. We convolve this uncertainty with the aforementioned 10% flux-calibration uncertainty in our analysis.

To measure upper-limit fluxes for nondetected emission lines, we assume a linewidth and an amplitude of 3 times the standard deviation of a continuum-subtracted line-free region of the spectrum. For H_2 lines, we assume the same linewidth as the narrow component of $H_2(1-0)\,S(1)$, the brightest H_2 line. For He I and $Br\gamma$, we adopt a linewidth of $130\,km\,s^{-1}$, based roughly on the average linewidth of the narrow component of optical ionized gas emission lines from T. A. Davis et al. (2012).

We find that there is a sky oversubtraction feature near $Br\gamma$. To ensure that this feature does not impact our measured $Br\gamma$ fluxes, we determine the channels where this feature is present by comparing spectra across the cube, including in regions without any $Br\gamma$ emission. Because this feature is only on the edge of the $Br\gamma$ line profile, we mask these contaminated channels and fit $Br\gamma$ without severely impacting the Gaussian fit and resulting flux measurement.

To fit all spaxels in our data cube, we traverse the cube in a spiral starting from the center, and use the previous fit values as starting values for fitting the next spaxel.

3. Results

3.1. Detected Lines

We detect seven rovibrational H_2 emission lines and $Br\gamma$ in the nucleus of NGC 1266. Figure 1 shows the K-band NIFS spectrum of NGC 1266 extracted within a circular aperture at the center of the galaxy with a diameter of $100\,pc$ ($0.7''$). Highlighted regions show the eight detected emission lines, with an inset for each, showing a two-component Gaussian fit to the emission line. Two Gaussian components are required to fit the line profiles as shown in Figure 1, where a wide, blueshifted component is detected in the brightest H_2 lines.

Selected results of the full data-cube Gaussian fitting are shown in Figure 2. The left panel is an integrated flux map of the line-free region at $2.09\,\mu m$. The middle panel shows the fitted $H_2(1-0)\,S(1)$ flux map, the brightest H_2 emission line. The three circles in this panel are three different apertures used in later analysis to show the emission-line properties in different regions: east, west, and center. These apertures are chosen to sample different spatial regions of the shock and outflow: the nucleus and the two extended wings of H_2 emission. Finally, the third panel shows the fitted $Br\gamma$ flux map. Spaxels with a $Br\gamma$ signal-to-noise ratio (S/N) < 3 are not shown. A thin line on the west side visible in all three images is a detector artifact, so we avoid this region in the west aperture and neglect the bright $Br\gamma$ emission on the edge of the detector.

We measure fluxes in each aperture by summing the spectra and fitting two Gaussian components as described in Section 2.2. Table 2 shows the measured fluxes for each emission line in each aperture and across the NIFS field of view. We do not detect the He I $2.06\,\mu m$ emission line in any of our apertures or summing across the entire field of view, so we report measured upper limits. Flux uncertainties reported in this table are from fitting only and do not include flux-calibration uncertainties. We repeat our analysis with nonparametric fluxes measured by summing the continuum-subtracted spectra within $\pm 800\,km\,s^{-1}$ of each line, and find similar, though noisier, results.

We repeat our analysis with apertures chosen at different locations across the NIFS field of view and find little variation in our results. Therefore, we have only plotted the three apertures shown in Figure 2 as these apertures are representative and they have a high S/N.

3.2. H_2 Kinematics

We plot our measured velocities and linewidths from our two-component Gaussian fitting described in Section 2.2 in Figure 3. We begin by setting the narrower Gaussian component as component 1, and broader Gaussian component as component 2. However, in the southwest region, the widths of the two components are similar, so we select the higher-velocity, redshifted
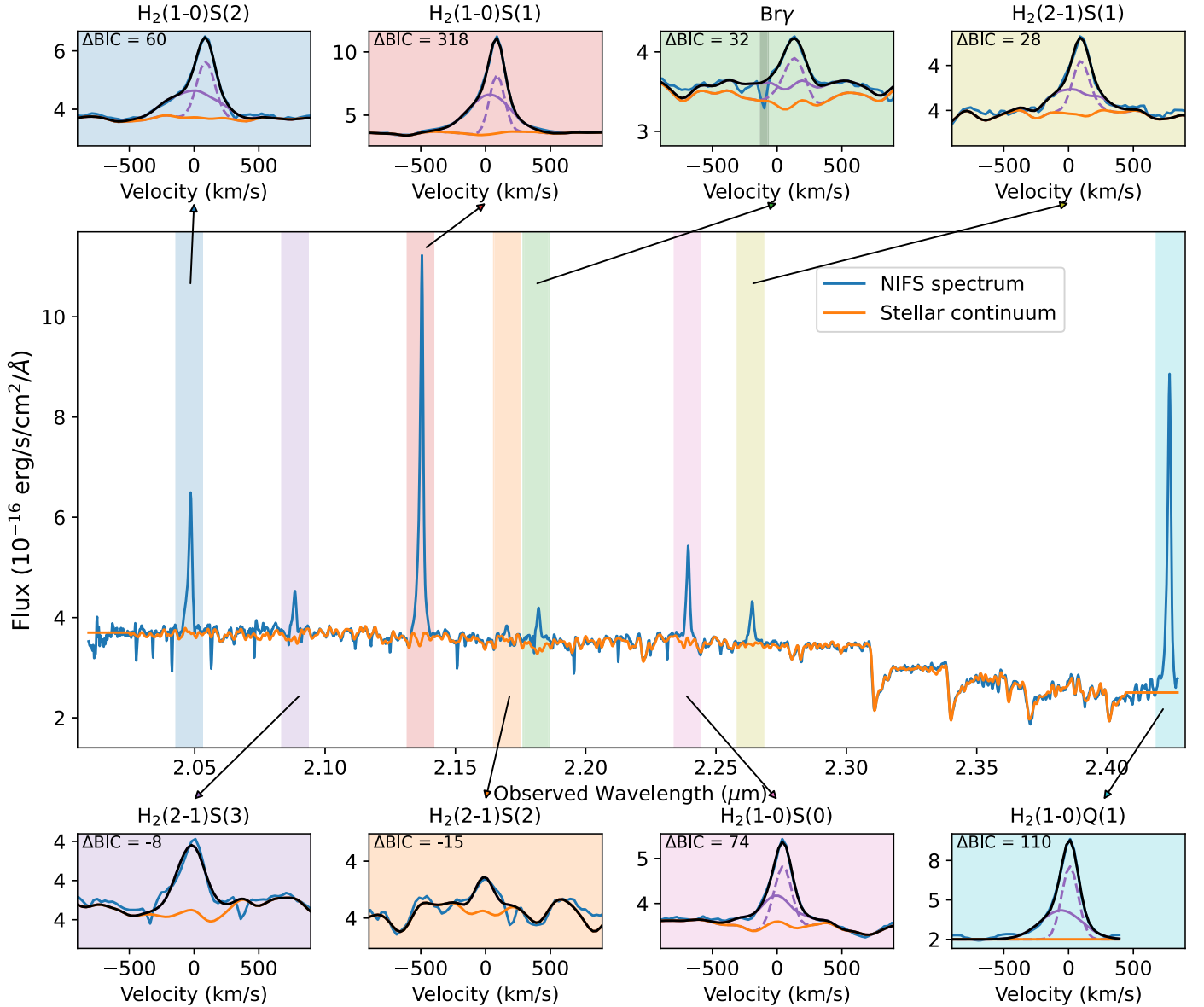
Figure 1. *K*-band spectrum of the central 100 pc of NGC 1266 from Gemini-NIFS. The surrounding axes show zoom-ins of detected emission lines where the colors of the axes show the corresponding location in the spectrum. The purple lines show each fitted Gaussian component, and the orange line is the linear continuum fit. The black line is the total two-component Gaussian and continuum fit. In the Brγ panel, the gray shaded region shows points masked out due to sky oversubtraction.

component as component 1 to maintain continuity in the velocity fields. The narrower component is the systemic component, as its velocity field is broadly similar to that of the stellar velocity field from optical IFS stellar fitting (T. A. Davis et al. 2012). The second component corresponds to the outflow as the position angle of the velocity field is similar to previous observations of the outflow (K. Alatalo et al. 2011; T. A. Davis et al. 2012), and the greater velocities and velocity widths are consistent with an outflow origin. The outflow reaches velocities of $400\,\mathrm{km\,s^{-1}}$, greater than the $\lesssim 100\,\mathrm{km\,s^{-1}}$ of the systemic component. The width of the outflow component reaches linewidths up to $300\,\mathrm{km\,s^{-1}}$, whereas the narrow systemic component remains around $75\,\mathrm{km\,s^{-1}}$.

3.3. Brγ Emission

In the central 100 pc aperture, we measure a Brγ flux of $6.8 \times 10^{-16}\,\mathrm{erg\,s^{-1}cm^{-2}}$. We apply an extinction correction from spatially unresolved Paβ and Brγ measurements from

R. Riffel et al. (2013). We measure the visual extinction by assuming an intrinsic Paβ/Brγ ratio of 5.89, corresponding to case B recombination, $n_e = 10^4\ \mathrm{cm^{-3}}$, and $T = 10^4\,\mathrm{K}$ (D. E. Osterbrock & G. J. Ferland 2006):

$$A_V = 11.52 \log\left(\frac{5.89}{F_{\mathrm{Br\gamma,obs}}/F_{\mathrm{Pa\beta,obs}}}\right), \qquad (3)$$

yielding $A_V = 12$. We use the J. A. Cardelli et al. (1989) extinction curve with $R_V = 3.1$, to find a Brγ extinction of 1.4. Thus, we obtain an extinction-corrected Brγ flux of $2.4 \times 10^{-15}\,\mathrm{erg\,s^{-1}\,cm^{-2}}$, or an extinction-corrected luminosity of $2.8 \times 10^{38}\,\mathrm{erg\,s^{-1}}$.

We stress that this extinction correction is a lower limit. Spitzer observations show a silicate optical depth of $\tau_{9.7\,\mu m} = 2.05$ (J. D. T. Smith et al. 2007; E. W. Pellegrini et al. 2013), which corresponds to a *V*-band extinction of $A_V \sim 34$ (G. H. Rieke & M. J. Lebofsky 1985). This extinction
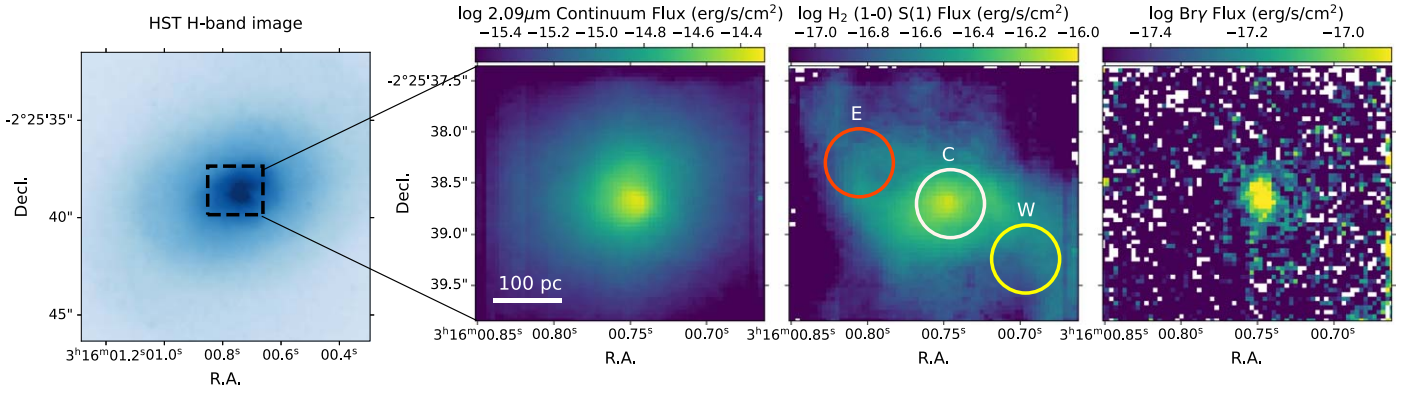
Figure 2. Left: HST *H*-band image of NGC 1266. The black dashed rectangle shows the Gemini-NIFS field of view. Center left: NIFS log 2.09 μm continuum flux map. The continuum is measured in a line-free spectral region. Center right: log H_2 (1–0) S(1) flux map. The three circles show three apertures extracted. Each aperture has a physical radius of 50 pc, and is labeled "W," "E," or "C." Line fluxes are measured by summing the two fitted Gaussian components and are continuum-subtracted. Right: Brγ flux map.

Table 2
Measured Line Fluxes for the Three Apertures Shown in Figure 2

Line	Rest Wavelength (μm)	Center Flux (10^{-16} erg s^{-1} cm^{-2})	West Flux (10^{-16} erg s^{-1} cm^{-2})	East Flux (10^{-16} erg s^{-1} cm^{-2})	FOV Flux (10^{-16} erg s^{-1} cm^{-2})
H_2(1–0)S(2)	2.0332	38.1 ± 0.6	16.01 ± 0.27	15.0 ± 0.15	298 ± 5
He I	2.0587	<50.0	<19.64	<19.45	<346.0
H_2(2–1)S(3)	2.0735	13.1 ± 0.3	3.99 ± 0.1	3.62 ± 0.14	74 ± 2
H_2(1–0)S(1)	2.1213	96.8 ± 0.6	40.2 ± 0.2	40.52 ± 0.16	742 ± 5
H_2(2–1)S(2)	2.1542	3.3 ± 0.2	0.82 ± 0.08	1.1 ± 0.12	16 ± 2
Brγ	2.1654	20.2 ± 0.8	1.24 ± 0.12	1.05 ± 0.1	44 ± 2
H_2(1–0)S(0)	2.223	24.9 ± 0.7	8.96 ± 0.25	8.48 ± 0.17	177 ± 5
H_2(2–1)S(1)	2.247	12.6 ± 0.7	4.54 ± 0.22	6.08 ± 0.17	107 ± 6
H_2(1–0)Q(1)	2.4066	84.6 ± 0.7	13.08 ± 0.09	>25.5	>373

Note. Fluxes reported here are the sum of the flux of both fitted components when two components were used. The final column shows the measured fluxes over the entire field of view of the NIFS observations. Reported uncertainties do not include the 10% flux-calibration uncertainty. Lower limits are indicated where part of the emission line falls out of the spectrum.

measurement likely overestimates the extinction of the Brγ emission, as some regions of the nucleus may be optically thick in the NIR and thus inflate the mean silicate optical depth, while the majority of the Brγ emission could be from low-extinction regions. Further, this silicate optical depth measurement is extracted over a roughly circular aperture with a radius of $10''$, far larger than the field of view of the NIFS observations, and may therefore be contaminated by excess extinction outside of the nuclear region.

3.4. Rovibrational H_2 Excitation Diagrams

We can measure the excitation temperature of the hot H_2 traced by rovibrational emission. In Figure 4, we plot the upper-level excitation energy for each detected H_2 line against the column density normalized by the degeneracy for the transition. We compute the column density following M. J. F. Rosenberg et al. (2013):

$$\frac{N_{\rm obs}(\nu, J)}{g_J} = \frac{4\pi\lambda}{hc} \frac{I_{\rm obs}(\nu, \nu', J, J')}{A(\nu, \nu', J, J')} \frac{1}{g_J}, \qquad (4)$$

where $N_{\rm obs}(\nu, J)$ is the upper energy level (ν, J) column density, g_J is the degeneracy of this level, $I_{\rm obs}(\nu, \nu', J, J')$ is the observed flux of the transition, and $A(\nu, \nu', J, J')$ is the associated Einstein radiative transition probability from L. Wolniewicz et al. (1998). For thermally excited gas in local

thermodynamic equilibrium (LTE), the column densities in the excitation diagram will be linearly related to the energies with a single temperature (e.g., R. I. Davies et al. 2003).

To measure the excitation temperature of the molecular hydrogen, we linearly fit the excitation diagram considering all detected emission lines, and the (1–0) lines separately. For the central aperture, the combined linear fit yields a temperature of 2150 ± 100 K, while the fit to the (1–0) lines only has a steeper slope with a temperature of 1500 ± 400 K. Despite the large uncertainty on the (1–0)-only fit, the difference in slope indicates that the (2–1) energy levels are overexcited compared to LTE conditions. Thus, the nucleus likely contains gas at multiple temperatures that cannot be adequately described with a single temperature, where the lower-energy (1–0) levels are weighted toward lower temperatures. In the west and east apertures, the combined linear fit and the fit to only the (1–0) lines are similar, with excitation temperatures ranging from 2000 to 2200 K.

3.5. Ortho-to-Para Ratio

The ortho-to-para ratio (OPR) can be used as a diagnostic to aid in determining the excitation source of warm H_2. This ratio measures the amount of emission from ortho-H_2 molecules (i.e., where the nuclear spins are aligned) to that of para-H_2 (i.e., the spins are antialigned).
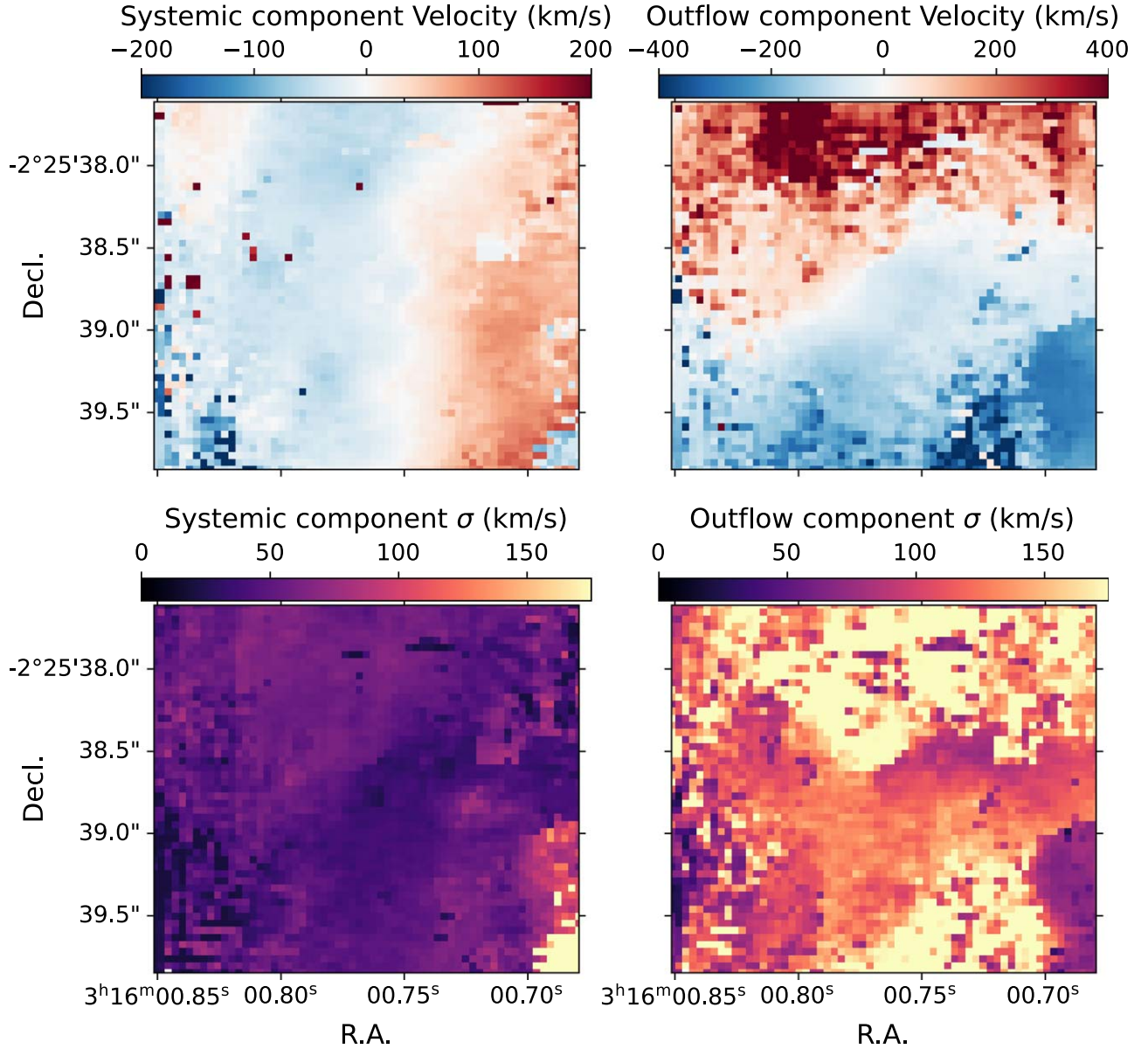
Figure 3. Fitted two-component kinematics of $H_2(1-0)S(1)$. The top row shows the velocity maps and the lower row the measured linewidth. The velocity field of the first component on the left is similar to the stellar velocity field, thus tracing the systemic gas rotation, while the second, broad component on the right traces the outflow and is misaligned from the systemic component.

We measure the rovibrational OPR in each aperture following A. Harrison et al. (1998). In the central, west, and east apertures we find OPRs of 2.6 ± 0.4, 2.8 ± 0.4, and 3.0 ± 0.5, respectively, for the $\nu = 1$ transitions (i.e., $(1-0)$ S(1)/(1-0) S(0)). All of these values are consistent with the equilibrium value of 3, within uncertainties. While an equilibrium value of the OPR typically indicates that the excitation source is thermal, it is possible for a dense photodissociation region (PDR) to have an OPR of 3 due to collisional de-excitation (A. Sternberg 1989; M. G. Burton et al. 1990).

3.6. H_2 Line Diagnostics

Various ratios of H_2 rovibrational lines provide useful diagnostics for determining the excitation mechanism of the gas. Figure 5 plots two line ratios: $(1-0)S(2)/(1-0)S(0)$ on the y-axis (a ratio of para transitions), and $(2-1)S(1)/(1-0)S(1)$ on

the x-axis (a ratio of ortho transitions). The ortho ratio is useful for differentiating between thermal, nonthermal, and mixed excitation mechanisms, whereas the para ratio is driven upward with increasing excitation temperature. We note that in a dense PDR, collisional de-excitation can drive the $(2-1)S(1)/(1-0)S$ (1) ratio lower, and thus it appears to be thermally excited (A. Harrison et al. 1998). We plot our three apertures in colored points, and additionally plot these line ratios for a sample of AGN (dark gray circles R. Riffel et al. 2013) and luminous infrared galaxies (LIRGs, light gray pentagons; V. U et al. 2019) for reference. We also include measurements for a shocked supernova remnant, IC 443 (Y. Deng et al. 2023). The black line shows the expected line ratios for a gas of uniform density in thermodynamic equilibrium. The two outer apertures of NGC 1266 are consistent with the purely thermally excited molecular gas at approximately 2000 K, as we might expect from shock excitation. The central aperture has a lower $H_2(1-0)$ S(2)/S(0) ratio, and is thus closer to bulk of the AGN and
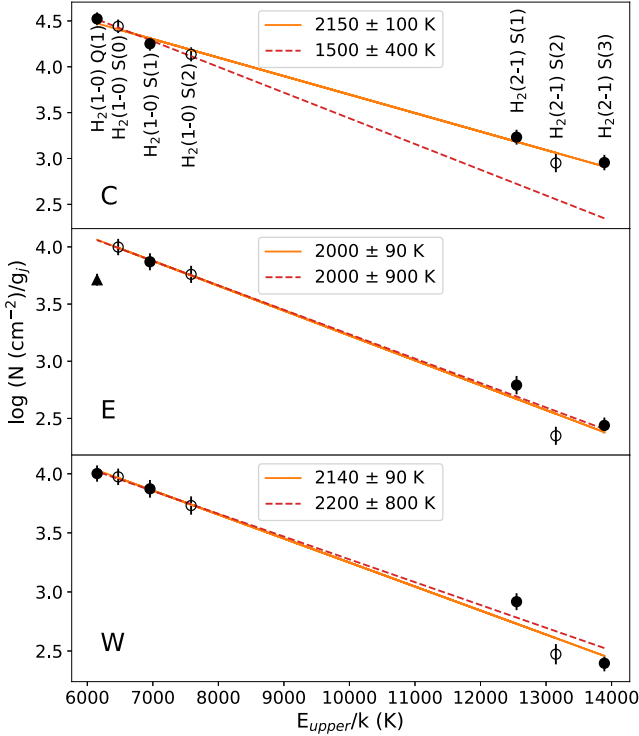
Figure 4. H_2 excitation diagram in the central, east, and west regions of NGC 1266. Open and filled circles correspond to para and ortho lines, respectively. The upward triangle in the east region indicates a lower limit. The orange line shows a linear fit for all plotted emission lines, and the dashed red line is a linear fit to the (1–0) transition lines only. In the central aperture (top), the difference in slope between the red and orange fits shows that the (2–1) levels are relatively overpopulated. In the east and west apertures (middle and lower), a higher temperature of ~2100 K is measured, and a single linear fit adequately describes the plotted transitions, indicating the gas is in LTE.

LIRG samples, indicating a possible PDR contribution to the excitation in the nucleus from either an AGN or starburst, as would be expected in AGN hosts and LIRGs.

Another important NIR diagnostic is shown in Figure 6, the $H_2(1\text{–}0)S(1)/Br\gamma$ ratio (hereafter $H_2/Br\gamma$ ratio). This ratio is useful for constraining the excitation mechanism by tracing the relative amounts of ionized gas and warm molecular gas. Star-forming galaxies tend to exhibit $H_2/Br\gamma < 0.4$, AGN lie in the range $0.4 < H_2/Br\gamma < 6$, and shocked regions have ratios >6 (R. Riffel et al. 2013). In the center of NGC 1266, we find an $H_2/Br\gamma$ ratio of 4.8 ± 0.7, whereas the east and west apertures have ratios of 32 ± 6 and 39 ± 7, respectively. While the H_2 line ratios discussed above have little spatial variation, the $H_2/Br\gamma$ varies significantly due to the centrally concentrated nature of the $Br\gamma$ emission, as shown in Figure 2. Comparing to other observational samples of galaxies, the center of NGC 1266 is consistent with the plotted LIRG and AGN samples, while the east and west measurements have values beyond nearly all other observed galaxies, and are consistent with shock excitation.

3.7. Warm Molecular Gas Masses

We compute the warm molecular gas mass from our $H_2(1\text{–}0)S(1)$ flux following X. Mazzalay et al. (2013). We assume a temperature $T = 2000$ K (as is consistent with our measurements in Figure 4), an $H_2(1\text{–}0)S(1)$ transition probability $A_{S(1)} = 3.47 \times 10^{-7}\,\text{s}^{-1}$, and a population fraction in the
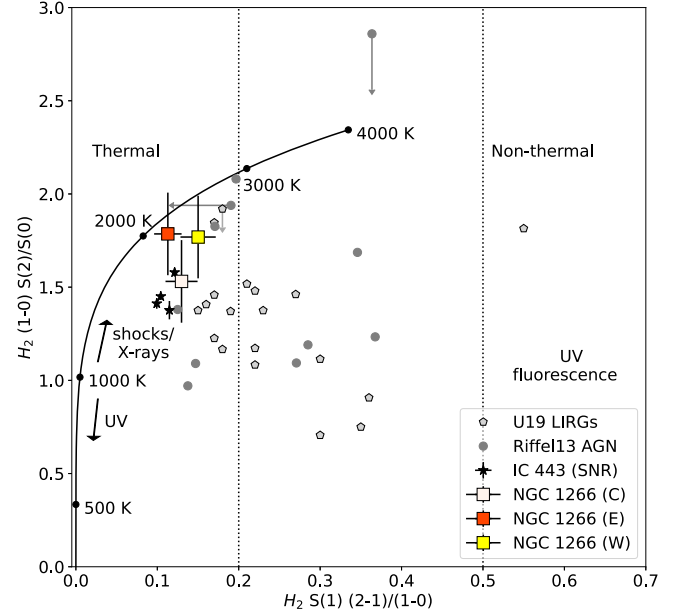

Figure 5. H_2 line ratio plot for extracted apertures of NGC 1266 and comparison samples. The orange, white, and yellow squares show the ratios in the three extracted apertures shown in Figure 2. The two outer apertures have similar H_2 line ratios, while the central aperture is farther from the black line showing the expected LTE line ratios at the labeled temperatures. UV photons account for excitation below 1000 K, while shocks and X-rays heat the gas above 1000 K. The nonthermal region on the right side shows line ratios for UV fluorescence from J. H. Black & E. F. van Dishoeck (1987). The black stars show the line ratios for IC 443 from Y. Deng et al. (2023), a shocked supernova remnant. The outlined pentagons show measurements from a sample of LIRGs from V. U et al. (2019), and the gray circles are a sample of AGN from R. Riffel et al. (2013).

$(\nu, J) = (1, 3)$ level of 0.0122. This yields the relation

$$M_{H_2,\text{warm}} \simeq 5.0875 \times 10^{13} \left(\frac{D}{\text{Mpc}}\right)^2 \left(\frac{F_{(1-0)S(1)}}{\text{erg s}^{-1}\,\text{cm}^{-2}}\right) 10^{0.4 A_{2.2}},$$

$$(5)$$

where $D = 29.9$ Mpc is the distance to NGC 1266, $F_{(1-0)S(1)}$ is the flux of the $H_2(1\text{–}0)S(1)$ line, and $A_{2.2}$ is the extinction at 2.2 μm. To derive $A_{2.2}$, we use the measured A_V from R. Riffel et al. (2013), as in Section 3.3, and adopt the same $R_V = 3.1$. We report our measured masses in Table 3. We again note that the extinction derived in Section 3.3 from the Paα to Brγ is likely an underestimate of the true extinction, and thus these measured gas masses should be considered lower limits.

4. Discussion

4.1. H_2 Excitation Mechanisms

Overall, our results demonstrate that the east and west regions are thermally excited by shocks, while we find evidence of an additional excitation mechanism in the nucleus. The excitation diagrams of the east and west apertures (see Figure 4) are well fit by a single temperature component of ~2100 K, consistent with thermal excitation at a single temperature. In the nucleus, the increase in temperature when fitting all detected H_2 transitions instead of only the (1–0) transitions indicates that the gas is not well described by a single temperature component because the (2–1) transitions are overpopulated relative to the (1–0) transitions. The lack of a

Table 3
Computed Quantities in Each Aperture and Across the Entire Field of View of the NIFS Observations

	Center	West	East	Entire FOV
Warm H_2 mass $(M_\odot)$[a]	1540 ± 150	640 ± 60	650 ± 60	$11{,}800 \pm 1{,}200$
Ortho-to-para ratio[b]	2.6 ± 0.4	2.8 ± 0.4	3.0 ± 0.5	2.7 ± 0.4
H_2/Brγ ratio[c]	4.8 ± 0.7	32 ± 6	39 ± 7	17 ± 3
$L_{Br\gamma}$ (10^{38} erg s^{-1})[d]	8.4 ± 0.9	0.52 ± 0.07	0.44 ± 0.06	18 ± 2
SFR ($M_\odot$ yr^{-1})[e]	0.69 ± 0.07	0.042 ± 0.005	0.036 ± 0.005	1.51 ± 0.17

Notes. Reported uncertainties include the 10% flux-calibration uncertainty.
[a] Measured warm H_2 masses calculated according to Equation (5).
[b] H_2 $\nu = 1$ ortho-to-para ratio.
[c] Ratio of H_2(1–0)S(1)/Brγ.
[d] Dust-corrected Brγ luminosity.
[e] Dust-corrected Brγ star formation rate, assuming all Brγ is from star formation.
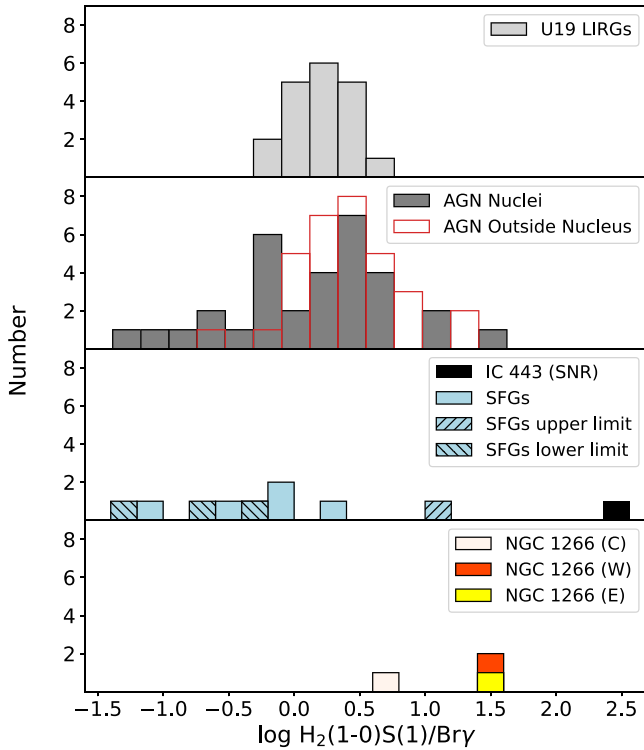
Figure 6. Histograms of the log H_2(1–0)S(1)/Brγ ratio for various samples. The top panel shows the LIRG sample from V. U et al. (2019). The next panel is the AGN sample from R. A. Riffel et al. (2021). The AGN nuclei are plotted in dark gray bars, where the nuclei measurements are within the central point-spread function FWHM (mean of 60 pc). The red outline shows the measurements from the same sample but outside the nuclear region plotted in gray. The third panel shows a sample of star-forming galaxies from D. A. Dale et al. (2004) in light blue bars. Diagonally hatched bars show upper- and lower-limit measurements. We also show the measurement from IC 443, a shocked supernova remnant (Y. Deng et al. 2023). In the bottom panel, we show the measurements from the three NGC 1266 apertures. The east aperture in yellow is a lower limit as Brγ is not detected.

single temperature component may indicate that there is either a contribution to the emission-line flux from a nonthermal excitation mechanism such as UV fluorescence, or multiple temperature components are present.

From comparisons with other galaxies, the overpopulated (2–1) transitions in the nucleus would be consistent with an excitation contribution from either AGN emission or star formation. Similar rovibrational excitation diagrams have been observed in both starburst and AGN host galaxies (M. J. F. Rosenberg et al. 2013; B. H. C. Emonts et al. 2014). The nuclear excitation diagram of NGC 1266 is especially similar to the excitation diagram of the southern, obscured nucleus of NGC 3256—a dual-AGN host galaxy with a likely AGN-driven outflow (B. H. C. Emonts et al. 2014). In that object, both nuclei have similar excitation temperatures of ~ 2000 K when fitting all transitions, and ~ 1600 K when only fitting the (1–0) transitions. B. H. C. Emonts et al. (2014) conclude that the molecular gas in NGC 3256 is likely heated to the observed temperature of 2000 K by either slow shocks or X-rays (potentially originating from the AGN). In NGC 1266, a contribution from both shocks and X-rays from the AGN could explain the observed departure from a single excitation temperature observed in shock-dominated systems.

Line ratio diagnostics further support a dominant thermal excitation mechanism heating the gas to a single excitation temperature in the outskirts, with a nonshock contribution in the nucleus. In the H_2 ratio diagram shown in Figure 5, purely thermal excitation has (2–1)S(1)/(1–0)S(1) $\lesssim 0.2$, and nonthermal has (2–1)S(1)/(1–0)S(1) $\gtrsim 0.5$ (J. H. Black & E. F. van Dishoeck 1987; P. W. J. L. Brand et al. 1989; B. T. Draine & D. T. Woods 1990; H. Mouri 1994; R. A. Dors et al. 2012). The ratio of para transitions, (1–0)S(2)/(1–0)S(0), increases with higher excitation temperatures and can distinguish between thermal UV excitation and shock or X-ray excitation as UV excitation does not heat the molecular gas above ~ 1000 K (A. Sternberg 1989). The west and east NGC 1266 apertures lie along the expected LTE relation above 2000 K, while the central aperture is offset below this line and is closer to the majority of the LIRG sample of V. U et al. (2019). The outer apertures thus are consistent with shock or X-ray excitation, while the offset below the LTE relation is consistent with a nonshock contribution in the center. In comparison to the AGN sample of R. Riffel et al. (2013) and the LIRG nuclei sample of V. U et al. (2019), NGC 1266 occupies a relatively unpopulated region of this diagram, where the many galaxies in these other samples appear to have some nonthermal contribution to their H_2 excitation, likely from UV fluorescence originating from AGN or star formation. The high H_2/Brγ ratio shown in Figure 6 further supports shock excitation in the east and west apertures outside the nucleus, while the center has some star formation or AGN contribution.

Finally, the observed H_2 OPR of 3 is consistent with a thermal excitation mechanism including shocks. Hydrogen molecules can be excited into different quantum states through reactive collisions with protons or hydrogen atoms. While the OPR is initially set by H_2 formation mechanisms, once the gas reaches LTE and has

$T > 200$ K, the equilibrium OPR is 3. However, if the H_2 is excited from far-UV (FUV) pumping and only vibrationally excited states (i.e., $\nu \geqslant 1$) are considered, the equilibrium OPR is 1.7 (A. Sternberg 1989). In a PDR where FUV pumping is present, the observed OPR is expected to lie near this value. However, in a dense PDR, collisional de-excitation of H_2 can drive the OPR to the equilibrium value. *K*-band observations of starburst galaxies have yielded subequilibrium OPR values, indicating that the excitation has contributions both from a thermal source (shocks or UV irradiation) and FUV pumping (A. Harrison et al. 1998; R. I. Davies et al. 2003). Our observed OPRs of 3 therefore do not disqualify the possibility of excitation from a dense PDR, but are consistent with our conclusion that the H_2 is primarily excited by shocks.

4.2. Shock Diagnostics

Insight into the properties of the shock in NGC 1266 is crucial to understanding how the shock is propagating through the galaxy and the impact it has on the ISM. Previous shock modeling of expected H_2 rovibrational and Brγ emission can help characterize the shock properties in NGC 1266. Shocks are typically described as either continuous (C-shocks) or jump (J-shocks), where continuous shocks are modeled with continuously varying properties such as temperature and density and jump shocks have a discontinuous change in properties at the shock front. The NIR spectral properties of four classes of shocks can be summarized as the following (M. G. Burton et al. 1990; R. Davies et al. 2000):

 (i) Fast J-shocks (v from 100 to 300 km s^{-1}) are highly dissociative, resulting in similar Brγ and H_2(1–0)S(1) fluxes.
 (ii) Slow J-shocks (v from 5 to 15 km s^{-1}) are not dissociative, resulting in strong H_2 emission and weak Brγ, and high post-shock gas temperatures around 4000 K. Typically, these shocks will revert to a C-shock (D. Hollenbach & C. F. McKee 1989).
 (iii) Fast C-shocks (v from 25 to 40 km s^{-1}) would heat the gas from 1000 to 3000 K depending on the shock velocity, resulting in strong H_2 emission and little Brγ as these shocks are not strongly dissociative.
 (iv) Slow C-shocks ($v \leqslant 15$ km s^{-1}) only heat the gas to ~ 300 K with weak H_2 emission.

Thus, our observed gas temperature of ~ 2000 K and high H_2/Brγ ratio are most consistent with a fast C-shock.

Previous studies of the shocks in NGC 1266 have relied on MIR H_2 pure rotation lines and the CO and H_2O spectral line energy distributions, and find that a C-shock with $n_H = 10^4$ cm^{-3} and $v_s = 25$–30 km s^{-1} is most consistent with these observations (E. W. Pellegrini et al. 2013; P. Chen et al. 2023). Both analyses require a contribution from PDRs in addition to shocks to reproduce the observed fluxes, which is expected as the observations were not spatially resolved and thus had no differentiation between the central core and the surrounding region. Comparing to NIR shock models, we find that these derived shock properties from the MIR are consistent with our observed NIR H_2 and Brγ emission.

4.3. Resolved Shock Structure

In Figure 2, we resolve the structure of the shock in the central 450 pc of NGC 1266 with an unambiguous shock tracer

for the first time. The H_2 flux shows a clear structure extending from the northwest to the southeast. While the morphology of the H_2 emission may have implications for the physical mechanism driving the shocks (i.e., radio jets or supernovae), it is difficult to make conclusions without accompanying multiwavelength observations at similar spatial resolution. Forthcoming high-resolution Very Large Array (VLA) observations of NGC 1266 will be presented in J. A. Otter et al. (2024, in preparation) and may clarify whether the shocked molecular gas is a product of jet–ISM interaction.

4.4. Star Formation or AGN?

Our results show that the excitation source in the central 100 pc is different from the surrounding region. While the outskirts show clear signs of shock excitation, the center appears to have some contribution from another mechanism as the (2–1) levels are elevated above the thermalized temperature of the (1–0) levels (see Figure 4). Moreover, the central region has an H_2/Brγ ratio consistent with AGN nuclei and LIRGs in Figure 6, while Brγ is either undetected or weak in the east and west spectra. Either AGN emission or central star formation may be responsible for the Brγ emission.

To unambiguously determine whether the central energy source is dominated by the AGN or star formation, a reliable measurement of the AGN bolometric luminosity is needed. K. Alatalo et al. (2015) first estimate the AGN bolometric luminosity by extrapolating from the IR luminosity of the compact central source and a full spectral energy distribution (SED) fit, finding $L_{bol} = 3.4 \times 10^{43}$ erg s^{-1}. However, a reanalysis of the full SED by P. Chen et al. (2023) finds a lower AGN contribution to the IR luminosity, and a resulting lower total luminosity of $L_{bol} = 1.25 \times 10^{42}$ erg s^{-1}.

We can roughly estimate the AGN contribution to the central Brγ emission for these differing L_{bol} measurements using the empirical L_{bol}–$L_{H\alpha}$ relation (J. E. Greene & L. C. Ho 2007), and then converting the expected Hα luminosity to Brγ by assuming Case B recombination and the same gas properties as in Section 3.3. Using the K. Alatalo et al. (2015) L_{bol}, the expected Brγ luminosity from the AGN is 10^{39} erg s^{-1}, which is slightly higher than our measured Brγ luminosity. If the K. Alatalo et al. (2015) measure of L_{bol} is correct, this discrepancy could be due to an underestimate of the dust extinction from the lower-spatial-resolution R. Riffel et al. (2013) observations.

Alternatively, if we adopt the L_{bol} from P. Chen et al. (2023), we find that the AGN contributes little to the Brγ emission, and thus that the Brγ emission is almost entirely due to central star formation. For $L_{bol} = 1.25 \times 10^{42}$ erg s^{-1}, the expected Brγ luminosity is 2.2×10^{37} erg s^{-1}, well over an order of magnitude below our measured Brγ luminosity. In this scenario, we assume the Brγ emission is purely star formation, and measure a nuclear star formation rate of $0.69 \pm 0.07\, M_\odot$ yr^{-1} using the adjusted R. C. Kennicutt (1998) Hα star formation law presented by V. U et al. (2019), though we note that we may be underestimating the dust extinction, as discussed in Section 3.3.

While a variety of multiwavelength star formation tracers yield measurements spanning an order of magnitude, this Brγ measurement constrains the ongoing star formation on the timescale of the outflow. The outflow appears to have originated $\lesssim 5$ Myr ago (T. A. Davis et al. 2012), and with a recent burst of star formation within the last ~ 500 Myr, tracing the star formation
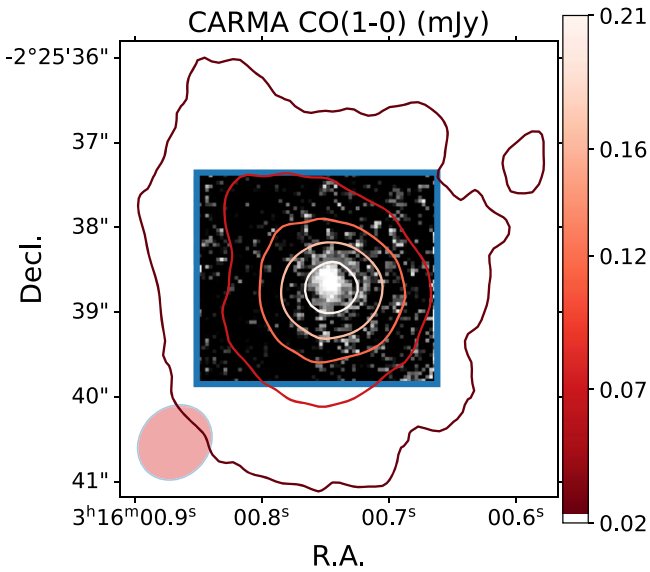
Figure 7. Brγ flux map, with the NIFS field of view shown with the blue rectangle. The red contours show CARMA CO(1–0) observations from K. Alatalo et al. (2015). The red ellipse shows the CARMA beam size. Though at coarser resolution than the NIFS data, the CO extent is much larger than the Brγ emission.

on short timescales is crucial for identifying the impact of the outflow on the star formation. K. Alatalo et al. (2015) perform an exhaustive study of star formation tracers in NGC 1266, finding a range of values from ∼0.3 to ∼2.2 $M_\odot$ yr^{-1}. While such a discrepancy may appear alarming, every individual star formation tracer has a unique combination of contaminants (primarily AGN emission and shocks), suppressants (e.g., dust extinction and dust destruction), and, crucially, trace star formation on different timescales.

A variety of star formation tracers in other post-starburst galaxies also yield a wide range of values, likely due to differing timescales probed and contamination (A. Smercina et al. 2018; Y. Luo et al. 2022). Star formation tracers that originate from ionized H II regions surrounding young stars trace star formation on timescales of order the lifetime of massive stars, ∼10 Myr (e.g., J. P. Ostriker et al. 1974). Hydrogen recombination lines and forbidden emission lines in particular provide an excellent probe of existing H II regions, though they can be significantly contaminated by shocks. K. Alatalo et al. (2015) measure the star formation rate of NGC 1266 with the mid-infrared (MIR) [Ne II] 12 μm and [Ne III] 15 μm emission lines of ≈1.5 $M_\odot$ yr^{-1}. While MIR emission lines have the advantage of little dust extinction, this derived star formation rate may be heavily contaminated by shocks or the AGN, and the Spitzer observations these measurements are made from lack the spatial resolution to resolve the morphology of this emission.

The most robust star formation tracer from K. Alatalo et al. (2015) is the free–free emission originating from H II regions, yielding a star formation rate of 0.87 $M_\odot$ yr^{-1}, consistent with our measurement within uncertainties assuming all Brγ emission is from star formation. The free–free measurement has the advantage of having little dust extinction, though it lacks spatial information as the full SED fitting required to derive the free–free contribution uses photometry from observations with a variety of angular resolutions. We stress that each star formation tracer provides different physical

information and is subject to significant uncertainties, and that multiple tracers should be considered when constraining the star formation rate. High-resolution MIR and radio observations are needed to progress in disentangling the multiple energetic processes, unusual stellar population, and high extinction in this galaxy.

We compare the Brγ emission morphology to that of the CARMA CO(1–0) observations from K. Alatalo et al. (2015) in Figure 7. We see that the CO emission extends far beyond the Brγ emission, consistent with scenario 2 in K. Alatalo et al. (2015), where the majority of the molecular gas lacks significant star formation and the existing star formation is concentrated in a nuclear starburst. While it is unclear whether the source of the Brγ emission is this nuclear starburst or AGN, there is little star formation in the surrounding CO-emitting region of NGC 1266, indicating the vast majority of the molecular gas hosts suppressed star formation.

4.5. Implications for Star Formation Quenching

Our results show that NGC 1266 hosts a large reservoir of warm, shocked molecular gas in the central region with an extended shock morphology. We also find that the central 400 pc region has very little star formation, with the possible exception of a ≲100 pc nuclear star cluster.

K. Alatalo et al. (2015) propose two scenarios for star formation in NGC 1266: a nuclear starburst or distributed low-level star formation throughout the disk. Our results are thus consistent with the former, though it remains unclear precisely *why* this star formation is constrained only to the very nucleus and star formation suppressed elsewhere. This suppression is not solely due to a lack of cold molecular gas, as NGC 1266 hosts a significant reservoir of CO(1–0) over a ∼1 kpc extent (K. Alatalo et al. 2011). Though we find a significant amount of shock-heated molecular gas, K. Alatalo et al. (2015) detect multiple dense gas tracers such as CS(2–1) over a ∼500 pc extent, indicating that star formation is not suppressed due to a lack of available dense gas.

K. Alatalo et al. (2015) suggest that the outflow drives turbulence throughout the ISM of NGC 1266, effectively suppressing star formation. In this scenario, our results indicate that this star formation suppression is efficient, as the star formation in NGC 1266 is mostly relegated to the nucleus. In simulations and observations, excess turbulence has been shown to suppress star formation by increasing the virial parameter (i.e., the ratio between twice the kinetic to gravitational energy) in molecular clouds, thus making gravitational collapse more difficult. While turbulence can locally enhance star formation through local compression of gas, over larger volumes the increase in virial parameter has a greater impact, thus suppressing the star formation overall (C. Federrath & R. S. Klessen 2012; A. Mandal et al. 2021; C. Federrath et al. 2016; D. M. Salim et al. 2020).

Turbulent stabilization of the molecular gas may be a necessary component of star formation suppression mechanisms that do not rely on exhausting or expelling the molecular gas reservoirs. A number of studies have revealed that many post-starburst galaxies harbor significant cold molecular gas reservoirs despite their lack of star formation (K. D. French et al. 2015; K. Rowlands et al. 2015; J. A. Otter et al. 2022). High turbulence levels have been observed in a few post-starbursts, though the origin of this turbulence is unclear (A. Smercina et al. 2022). Outflows are often observed in post-starbursts, further

supporting that AGN feedback through outflows may play an important role in the evolution through the post-starburst phase and beyond (e.g., Y. Luo et al. 2022; J. A. Otter et al. 2022; A. Smercina et al. 2022; K. D. French et al. 2023).

5. Conclusions

In this work, we present K-band IFS observations of the central 500 pc of NGC 1266, yielding rovibrational H_2 emission maps, the first unambiguous shock tracer showing the morphology of the shock in this galaxy. This allows us to study the NIR nucleus at spatial high resolution, probing physical scales of $\lesssim$50 pc. We detect seven rovibrational H_2 emission lines and Brγ.

We make the following conclusions:

1. The H_2 rovibrational emission is primarily excited by a high-velocity C-shock, heating the molecular gas to approximately 2000 K, and the H_2 excitation properties are relatively uniform across the central $\sim$400 pc.

2. We have observed the morphology of the shock in the central region for the first time, though multiwavelength high-spatial-resolution observations are needed to determine the source of the shock.

3. The Brγ and H_2 excitation in the nucleus contains some contribution from a PDR originating from the AGN, star formation, or a combination of both.

4. If the Brγ emission in the nucleus is dominated by star formation, we measure a central star formation rate of $0.69 \pm 0.07\,M_\odot\,yr^{-1}$ (only including the formal uncertainty), consistent with previous short-timescale measurements of ongoing star formation. We note that the dust extinction may be higher than our estimate, and thus this star formation rate should be considered a lower limit, assuming little AGN contamination.

5. In either case, we observe little nonnuclear star formation in NGC 1266, indicating that the vast majority of the molecular gas has its star formation suppressed, potentially by turbulence driven by the outflow.

The multitude of physical processes ongoing in NGC 1266 make it an ideal laboratory for studying AGN feedback, star formation suppression, extragalactic shocks, jet–ISM interaction, and, most importantly, how all of these processes are intertwined. With the NIR observations presented here, we begin to resolve the structure of the shock for the first time, as is essential for uncovering the physics connecting the radio jets, to the outflows, to the shocks, and to the star formation. This work highlights the importance of spatially resolved studies of shock and star formation properties, as the excitation and gas properties in the central 100 pc are complex. Moving forward, high-spatial-resolution NIR and MIR observations over a large field of view with JWST are essential for fully characterizing the shock properties, structure, and the role of outflow-driven turbulence in star formation suppression. Further in the future, new radio telescopes with advancements in sensitivity and resolution, such as the next-generation VLA, will extend the work presented here to higher-redshift sources and enable statistical studies of the role of jet–ISM interactions in galaxy evolution (e.g., K. Nyland et al. 2018).

Appendix
H_2 Flux Maps

We present the results of our spaxel-by-spaxel two-component Gaussian fitting, as described in Section 2.2, for all detected H_2 lines in Figure 8. The eastern side of the $H_2(1$–$0)Q(1)$ map is empty as this region does not spectrally cover the entire emission line.
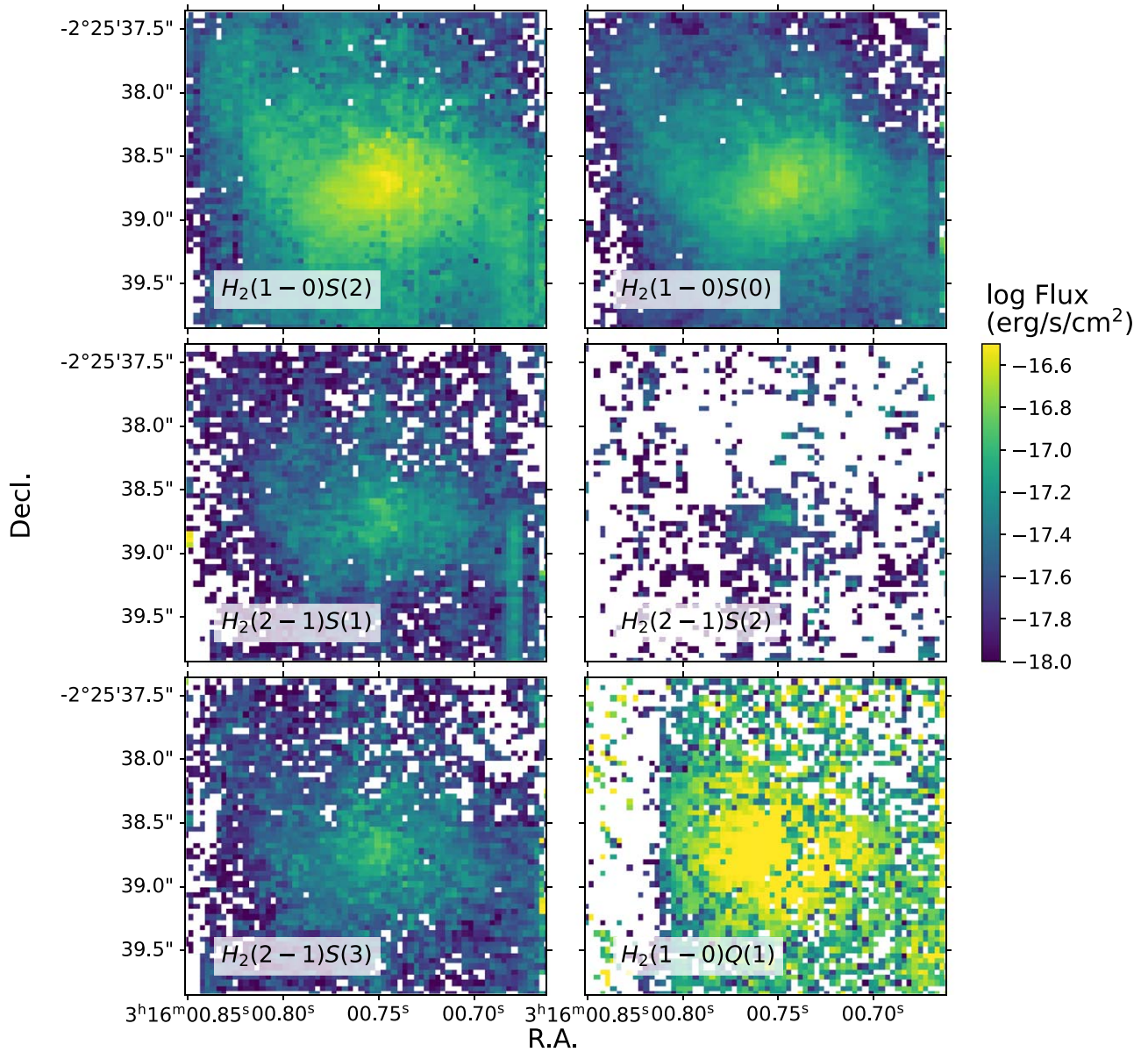
Figure 8. Flux maps for all detected H$_2$ emission lines. Line fluxes are the sum of both fitted Gaussian components and are continuum-subtracted. The empty east region in the H$_2$(1–0)Q(1) line is due to a lack of spectral coverage in that region.

ORCID iDs

Justin Atsushi Otter ⓘ https://orcid.org/0000-0003-3191-9039
Katherine Alatalo ⓘ https://orcid.org/0000-0002-4261-2326
Kate Rowlands ⓘ https://orcid.org/0000-0001-7883-8434
Richard M. McDermid ⓘ https://orcid.org/0000-0002-8175-7229
Timothy A. Davis ⓘ https://orcid.org/0000-0003-4932-9379
Christoph Federrath ⓘ https://orcid.org/0000-0002-0706-2306
K. Decker French ⓘ https://orcid.org/0000-0002-4235-7337
Timothy Heckman ⓘ https://orcid.org/0000-0001-6670-6370
Patrick Ogle ⓘ https://orcid.org/0000-0002-3471-981X
Darshan Kakkad ⓘ https://orcid.org/0000-0002-2603-2639
Yuanze Luo ⓘ https://orcid.org/0000-0002-0696-6952
Kristina Nyland ⓘ https://orcid.org/0000-0003-1991-370X
Akshat Tripathi ⓘ https://orcid.org/0000-0002-6582-4946
Pallavi Patil ⓘ https://orcid.org/0000-0002-9471-8499
Andreea Petric ⓘ https://orcid.org/0000-0003-4030-3455
Adam Smercina ⓘ https://orcid.org/0000-0003-2599-7524

Maya Skarbinski ⓘ https://orcid.org/0009-0004-0844-0657
Lauranne Lanz ⓘ https://orcid.org/0000-0002-3249-8224
Kristin Larson ⓘ https://orcid.org/0000-0003-3917-6460
Philip N. Appleton ⓘ https://orcid.org/0000-0002-7607-8766
Susanne Aalto ⓘ https://orcid.org/0000-0002-5828-7660
Gustav Olander ⓘ https://orcid.org/0000-0003-4830-9069
Elizaveta Sazonova ⓘ https://orcid.org/0000-0001-6245-5121
J. D. T. Smith ⓘ https://orcid.org/0000-0003-1545-5078

References

Alatalo, K., Blitz, L., Young, L. M., et al. 2011, ApJ, 735, 88
Alatalo, K., Lacy, M., Lanz, L., et al. 2015, ApJ, 798, 31
Alatalo, K., Nyland, K., Graves, G., et al. 2014, ApJ, 780, 186
Astropy Collaboration, Price-Whelan, A. M., Sipőcz, B. M., et al. 2018, AJ, 156, 123
Astropy Collaboration, Robitaille, T. P., Tollerud, E. J., et al. 2013, A&A, 558, A33
Bae, H.-J., Woo, J.-H., Karouzos, M., et al. 2017, ApJ, 837, 91

Barnes, A. T., Longmore, S. N., Battersby, C., et al. 2017, MNRAS, 469, 2263
Bîrzan, L., Rafferty, D. A., McNamara, B. R., Wise, M. W., & Nulsen, P. E. J. 2004, ApJ, 607, 800
Black, J. H., & van Dishoeck, E. F. 1987, ApJ, 322, 412
Brand, P. W. J. L., Toner, M. P., Geballe, T. R., et al. 1989, MNRAS, 236, 929
Burton, M. G., Geballe, T. R., Brand, P. W. J. L., & Moorhouse, A. 1990, ApJ, 352, 625
Cappellari, M. 2017, MNRAS, 466, 798
Cappellari, M. 2023, MNRAS, 526, 3273
Cappellari, M., & Emsellem, E. 2004, PASP, 116, 138
Cardelli, J. A., Clayton, G. C., & Mathis, J. S. 1989, ApJ, 345, 245
Chen, P., Zhao, Y., & Wang, J. 2023, RAA, 23, 015005
Cheung, E., Bundy, K., Cappellari, M., et al. 2016, Natur, 533, 504
Christou, J. C., Neichel, B., Rigaut, F., et al. 2010, Proc. SPIE, 7736, 77361R
Dale, D. A., Roussel, H., Contursi, A., et al. 2004, ApJ, 601, 813
Davies, R., Ward, M., & Sugai, H. 2000, ApJ, 535, 735
Davies, R. I., Sternberg, A., Lehnert, M., & Tacconi-Garman, L. E. 2003, ApJ, 597, 907
Davis, T. A., Krajnović, D., McDermid, R. M., et al. 2012, MNRAS, 426, 1574
Deng, Y., Zhang, Z.-Y., Zhou, P., et al. 2023, MNRAS, 518, 2320
Di Matteo, T., Springel, V., & Hernquist, L. 2005, Natur, 433, 604
Dors, O. L., Jr, Riffel, R. A., Cardaci, M. V., et al. 2012, MNRAS, 422, 252
Draine, B. T., & Woods, D. T. 1990, ApJ, 363, 464
Emonts, B. H. C., Piqueras-López, J., Colina, L., et al. 2014, A&A, 572, A40
Fabian, A. C. 2012, ARA&A, 50, 455
Federrath, C., & Klessen, R. S. 2012, ApJ, 761, 156
Federrath, C., Rathborne, J. M., Longmore, S. N., et al. 2016, ApJ, 832, 143
Fernández-Ontiveros, J. A., Dasyra, K. M., Hatziminaoglou, E., et al. 2020, A&A, 633, A127
French, K. D. 2021, PASP, 133, 072001
French, K. D., Smercina, A., Rowlands, K., et al. 2023, ApJ, 942, 25
French, K. D., Yang, Y., Zabludoff, A., et al. 2015, ApJ, 801, 1
French, K. D., Zabludoff, A. I., Yoon, I., et al. 2018, ApJ, 861, 123
Gabor, J. M., & Bournaud, F. 2014, MNRAS, 441, 1615
Gaspari, M., Melioli, C., Brighenti, F., & D'Ercole, A. 2011, MNRAS, 411, 349
Greene, J. E., & Ho, L. C. 2007, ApJ, 670, 92
Guillard, P., Boulanger, F., Pineau des Forêts, G., et al. 2012, ApJ, 749, 158
Harris, C. R., Millman, K. J., van der Walt, S. J., et al. 2020, Natur, 585, 357
Harrison, A., Puxley, P., Russell, A., & Brand, P. 1998, MNRAS, 297, 624
Harrison, C. M., Alexander, D. M., Mullaney, J. R., & Swinbank, A. M. 2014, MNRAS, 441, 3306
Heckman, T. M., & Best, P. N. 2014, ARA&A, 52, 589
Heckman, T. M., & Best, P. N. 2023, Galax, 11, 21
Hollenbach, D., & McKee, C. F. 1989, ApJ, 342, 306
Hopkins, P. F., Somerville, R. S., Hernquist, L., et al. 2006, ApJ, 652, 864
Hunter, J. D. 2007, CSE, 9, 90
Kauffmann, G., Colberg, J. M., Diaferio, A., & White, S. D. M. 1999, MNRAS, 303, 188
Kennicutt, R. C., Jr. 1998, ApJ, 498, 541

Kwan, J. H., Gatley, I., Merrill, K. M., Probst, R., & Weintraub, D. A. 1977, ApJ, 216, 713
Lemoine-Busserolle, M., Comeau, N., Kielty, C., Klemmer, K., & Schwamb, M. E. 2019, AJ, 158, 153
Lepp, S., & McCray, R. 1983, ApJ, 269, 560
Luo, Y., Rowlands, K., Alatalo, K., et al. 2022, ApJ, 938, 63
Mandal, A., Mukherjee, D., Federrath, C., et al. 2021, MNRAS, 508, 4738
Martin, D. C., Wyder, T. K., Schiminovich, D., et al. 2007, ApJS, 173, 342
Mazzalay, X., Saglia, R. P., Erwin, P., et al. 2013, MNRAS, 428, 2389
McGregor, P. J., Hart, J., Conroy, P. G., et al. 2003, Proc. SPIE, 4841, 1581
Morganti, R., Fogasy, J., Paragi, Z., Oosterloo, T., & Orienti, M. 2013, Sci, 341, 1082
Mouri, H. 1994, ApJ, 427, 777
Mukherjee, S., Feigelson, E., Jogesh Babu, G., et al. 1998, ApJ, 508, 314
Nesvadba, N. P. H., Boulanger, F., Lehnert, M. D., Guillard, P., & Salome, P. 2011, A&A, 536, L5
Nesvadba, N. P. H., Boulanger, F., Salomé, P., et al. 2010, A&A, 521, A65
Nesvadba, N. P. H., Lehnert, M. D., De Breuck, C., Gilbert, A., & van Breugel, W. 2007, A&A, 475, 145
Nyland, K., Harwood, J. J., Mukherjee, D., et al. 2018, ApJ, 859, 23
Nyland, K., Alatalo, K., Wrobel, J. M., et al. 2013, ApJ, 779, 173
Osterbrock, D. E., & Ferland, G. J. 2006, Astrophysics of Gaseous Nebulae and Active Galactic Nuclei (Sausalito, CA: University Science Books)
Ostriker, J. P., Richstone, D. O., & Thuan, T. X. 1974, ApJ, 188, L87
Otter, J. A., Rowlands, K., Alatalo, K., et al. 2022, ApJ, 941, 93
Pellegrini, E. W., Smith (PI), J. D., Wolfire, M. G., et al. 2013, ApJ, 779, L19
Rieke, G. H., & Lebofsky, M. J. 1985, ApJ, 288, 618
Riffel, R., Rodríguez-Ardila, A., Aleman, I., et al. 2013, MNRAS, 430, 2002
Riffel, R. A., Storchi-Bergmann, T., Riffel, R., et al. 2021, MNRAS, 504, 3265
Rosenberg, M. J. F., van der Werf, P. P., & Israel, F. P. 2013, A&A, 550, A12
Rowlands, K., Wild, V., Nesvadba, N., et al. 2015, MNRAS, 448, 258
Roy, N., Bundy, K., Cheung, E., et al. 2018, ApJ, 869, 117
Rupke, D. S. N., Gültekin, K., & Veilleux, S. 2017, ApJ, 850, 40
Salim, D. M., Alatalo, K., Federrath, C., Groves, B., & Kewley, L. J. 2020, ApJ, 893, 26
Schawinski, K., Urry, C. M., Virani, S., et al. 2010, ApJ, 711, 284
Schaye, J., Crain, R. A., Bower, R. G., et al. 2015, MNRAS, 446, 521
Smercina, A., Smith, J. D. T., Dale, D. A., et al. 2018, ApJ, 855, 51
Smercina, A., Smith, o. T., French, K. D., et al. 2022, ApJ, 929, 154
Smethurst, R. J., Masters, K. L., Lintott, C. J., et al. 2018, MNRAS, 473, 2679
Smith, J. D. T., Draine, B. T., Dale, D. A., et al. 2007, ApJ, 656, 770
Sternberg, A. 1989, ApJ, 347, 863
U, V., Medling, A. M., Inami, H., et al. 2019, ApJ, 871, 166
Verro, K., Trager, S. C., Peletier, R. F., et al. 2022, A&A, 660, A34
Virtanen, P., Gommers, R., Oliphant, T. E., et al. 2020, NatMe, 17, 261
Vogelsberger, M., Genel, S., Springel, V., et al. 2014, Natur, 509, 177
Weinberger, R., Springel, V., Hernquist, L., et al. 2017, MNRAS, 465, 3291
Wild, V., Heckman, T., & Charlot, S. 2010, MNRAS, 405, 933
Wolniewicz, L., Simbotin, I., & Dalgarno, A. 1998, ApJS, 115, 293